



HAL
open science

Minibeam radiation therapy: a micro- and nano-dosimetry Monte Carlo study

M. dos Santos, R. Delorme, R. Salmon, Y. Prezado

► **To cite this version:**

M. dos Santos, R. Delorme, R. Salmon, Y. Prezado. Minibeam radiation therapy: a micro- and nano-dosimetry Monte Carlo study. *Medical Physics*, 2020, 47 (3), pp.1379-1390. 10.1002/mp.14009 . hal-02457183

HAL Id: hal-02457183

<https://hal.science/hal-02457183>

Submitted on 19 Aug 2020

HAL is a multi-disciplinary open access archive for the deposit and dissemination of scientific research documents, whether they are published or not. The documents may come from teaching and research institutions in France or abroad, or from public or private research centers.

L'archive ouverte pluridisciplinaire **HAL**, est destinée au dépôt et à la diffusion de documents scientifiques de niveau recherche, publiés ou non, émanant des établissements d'enseignement et de recherche français ou étrangers, des laboratoires publics ou privés.

1 Minibeam radiation therapy: a micro- and nano-dosimetry Monte Carlo study

2
3 M. Dos Santos^{*,1} and R. Delorme^{*,2,3}, R. Salmon^{2,3}, Y. Prezado^{2,3}.

4
5 ¹IRSN, Department of Radiobiology and regenerative medicine (SERAMED), Laboratory of Radiobiology
6 of Accidental exposures (LRAcc) Fontenay-aux-Roses.

7 ²Imagerie et Modélisation en Neurobiologie et Cancérologie (IMNC), CNRS, Univ Paris-Sud, Université
8 Paris-Saclay, F-91400 Orsay, France

9 ³Université de Paris, IMNC, F-91400 Orsay, France

10
11 *Co-first authors

12 Corresponding authors: morgane.dossantos@irsn.fr

13 Running title: MBRT: a micro- and nano-dosimetry study

14 15 **Abstract**

16 **Purpose:** Minibeam radiation therapy (MBRT) is an innovative strategy based on a distinct dose
17 delivery method that is administered using a series of narrow (submillimetric) parallel beams. To shed
18 light on the biological effects of MBRT irradiation, we explored the micro- and nanodosimetric
19 characteristics of three promising MBRT modalities (photon, electron, and proton) using Monte Carlo
20 (MC) calculations.

21 **Methods:** Irradiation with proton (100 MeV), electron (300 MeV), and photon (effective energy of
22 69 keV) minibeam were simulated using Geant4 MC code and the Geant4-DNA extension, which
23 allows the simulation of energy transfer points with nanometric accuracy. As the target of the
24 simulations, cells containing spherical nuclei with or without a detailed description of the DNA
25 geometry were placed at different depths in peak and valley regions in a water phantom. The energy
26 deposition and number of events in the cell nuclei were recorded in the microdosimetry study, and
27 the number of DNA breaks and their complexity were determined in the nanodosimetric study, where
28 a multi-scale simulation approach was used for the latter. For DNA damage assessment, an adapted
29 DBSCAN clustering algorithm was used. To compare the photon MBRT (xMBRT), electron MBRT
30 (eMBRT), and proton MBRT (pMBRT) approaches, we considered the treatment of a brain tumor
31 located at a depth of 75 mm.

32 **Results:** Both mean energy deposition at micrometric scale and DNA damage in the “valley” cell nuclei
33 were very low as compared with these parameters in the peak region at all depths for xMBRT and at
34 depths of 0 mm to 30 mm and 0 mm to 50 mm for eMBRT and pMBRT, respectively. Only the charged
35 minibeam were favorable for tumor control by producing similar effects in peak and valley cells after
36 70 mm. At the micrometer scale, the energy deposited per event pointed to a potential advantage of
37 proton beams for tumor control, as more aggressive events could be expected at the end of their
38 tracks. At the nanometer scale, all three MBRT modalities produced direct clustered DNA breaks,
39 although the majority of damage (> 93%) was composed of isolated single strand breaks. The pMBRT
40 led to a significant increase in the proportion of clustered single strand breaks and double-strand
41 breaks at the end of its range as compared to the entrance (7% at 75 mm vs. 3% at 10 mm) in contrast
42 to eMBRT and xMBRT. In the latter cases, the proportions of complex breaks remained constant,
43 irrespective of the depth and region (peak or valley).

44 **Conclusions:** Enhanced normal tissue sparing can be expected with these three MBRT techniques.
45 Among the three modalities, pMBRT offers an additional gain for radioresistant tumors, as it resulted

46 in a higher number of complex DNA damage clusters in the tumor region. These results can aid
47 understanding of the biological mechanisms of MBRT.

48 *Keywords: Minibeam Radiation Therapy, DNA damage, Monte Carlo simulations, GEANT4*

49

50 **1. Introduction**

51 The therapeutic index of radiation therapy (RT) treatments can be notably improved by changing the
52 dose delivery methods, such as the temporal¹ or spatial fractionation of the dose.²⁻⁸ Minibeam
53 radiation therapy (MBRT) is a promising example of how the spatial modulation of the dose can lead
54 to a net reduction in neurotoxicity^{2-5,7} while providing equivalent or superior tumor control to standard
55 RT for high-grade gliomas.^{6,8}

56 Although photon MBRT (xMBRT) was originally developed in synchrotrons,² it was recently
57 implemented on a cost-effective preclinical installation, the Small Animal Radiation Research Platform
58 (SARRP, XSTRAHL Ltd., UK), available at the Experimental Radiotherapy Platform of the Institut Curie
59 (Orsay, France).⁹ Recently, the promising potential of a combination of MBRT with charged particle
60 beams has started to be explored.¹⁰⁻¹³ Proton MBRT (pMBRT) was developed on a clinical beam line of
61 the Proton Therapy Center of the Institut Curie (ICPO, Orsay, France).^{7,14} Previous research
62 demonstrated significant widening of the therapeutic index^{7,8} when pMBRT was applied in preclinical
63 studies.^{14,15} This approach combines the advantages of spatial fractionation of the dose (i.e., sparing
64 of healthy tissue before the tumor) with the ballistic advantage of the Bragg peak and known superior
65 relative biological effectiveness of proton beams.¹⁶ Very high-energy electron (VHEE, i.e., 70-300 MeV)
66 therapy offers a potential alternative cost-effective solution to conventional radiotherapy beams.¹⁷
67 Among their major advantages over photons, one can retain the possibility to scan small pencil beams,
68 producing a finer resolution of intensity modulated treatment and favorable dosimetric characteristics
69 (i.e., low lateral penumbrae and reduced sensitivity to tissue heterogeneities) leading to superior dose
70 distributions in most clinical cases.¹⁸ The biological effectiveness of electron MBRT (eMBRT) has not
71 been evaluated, mainly due to a lack of available facilities. However, a theoretical proof of the concept
72 of VHEE grid-therapy has been reported.¹³ As VHEE with such high kinetic energy have a higher
73 probability to induce nuclear reactions, it is conceivable that their biological effect may be greater than
74 that of photons or clinical electrons.

75 The biological bases underlying these new RT approaches are not fully understood. Ionizing radiation
76 affects a diverse array of molecules and involves multiple (e.g., physical, chemical, and biological)
77 mechanisms at different space and time scales. The narrow beam sizes employed in MBRT exploit
78 dose-volume effects: the smaller the field size, the higher the tolerance of healthy tissue.^{19,20} According
79 to previous studies, hyperplasia and migration of endothelial and glial cells from valleys (low doses) to
80 peaks (high doses) led to recovery of damaged tissue.^{21,22} In addition, the preferential effect on
81 malignant tissue compared to normal tissue was attributed to MBRT-induced damage of the immature
82 tumor vasculature associated with tumor hypoxia and the lack of this effect on normal tissue.²³

83 The goal of this study was to expand understanding of the possible physical or biological mechanisms
84 involved in the response to MBRT irradiation. With this aim in mind, we explored the micro- and
85 nanodosimetric characteristics of three promising MBRT modalities (X-rays, VHEEs, and protons). The
86 impact of secondary and primary particles in peak or valley regions may differ markedly at micro- and
87 nanodosimetric scales. We performed the calculations using the Geant4 Monte Carlo (MC) code, and
88 especially the Geant4-DNA extension, allowing to simulate energy deposition by ionizing radiation in
89 very small biological structures, such as DNA, which is one of the most sensitive biological targets of
90 ionizing radiation. We undertook a theoretical microdosimetry study at the cell nucleus level (i.e.,

91 energy deposited, interaction probability, and peak-to-valley dose ratio [PVDR]) and an evaluation of
92 the number and complexity of DNA damage events induced at the nanometric scale.

94 **2. Materials and Methods**

95 *2.1. The Monte Carlo (MC) code*

96 The general-purpose Geant4 MC code^{24,25} (version 10.3 patch-01) and its extension, Geant4-DNA,^{26–29}
97 were used. Geant4-DNA allows the transportation of electrons in liquid water down to
98 thermalization.^{26–29} It can be used to simulate discrete interactions of electrons, protons, and neutral
99 hydrogen, as well as interactions of alpha particles and their charged states and some ions (Fe, C, O,
100 and N), in liquid water in micro- and nano-dosimetry studies. Simulations performed with this package
101 allow the calculation of all elementary interactions down to the electron-volt scale, with nanometric
102 accuracy. The calculations are performed on an event-by-event basis, taking into account all the energy
103 transfer points. In the present study, due to a lack of theoretical and experimental cross-section data
104 for biological molecules in condensed states, liquid water with five excitation levels and five ionization
105 shells was used as the target material.³⁰ For the sake of computation time, a combination of discrete
106 and condensed history processes was used in the MC calculations. The Geant4-DNA processes were
107 activated only in cells in order to let the short-range secondary particles be produced and tracked
108 precisely in the cytoplasm and cell nucleus, our sensitive target. Outside the cells, we used standard
109 low-energy electromagnetic and nuclear processes of Geant4 and applied a general tracking cut of
110 1 nm.^{24,25} We used the Livermore database for electromagnetic processes, which is well adapted for
111 low-energy interactions of electrons and photons down to 250 eV but also suitable for energies up to
112 1 GeV. Hadronic processes were those recommended in the *Hadrontherapy* advanced example of
113 Geant4. Inside de cells, the Geant4-DNA processes applied were those of the default physics
114 constructor “G4EmDNAPhysics” of the version 10.3 patch-01 of Geant4 code.^{26–28} As detailed in the
115 work of Bernal *et al.*²⁸, Geant4-DNA transports electrons, protons and Helium ions in the range of 7.4
116 eV to 1 MeV, 100 eV to 100 MeV and 1 keV to 400 MeV, respectively. Heavier ions are transported
117 only in the 0.5 MeV/u to 10⁶ MeV/u range. The photons are tracked following the Livermore database
118 even in the targets. We did not apply any additional energy user limits on the Geant4-DNA processes.
119 A model of a cell with or without a detailed description of DNA was introduced as the target of the
120 calculations and was placed at different depths in peak and valley regions.

122 *2.2. Simulation details of irradiation configurations, geometries and data recorded*

123 xMBRT, pMBRT and eMBRT were simulated using the irradiation configurations currently used for our
124 theoretical or experimental studies.^{5,14,31}

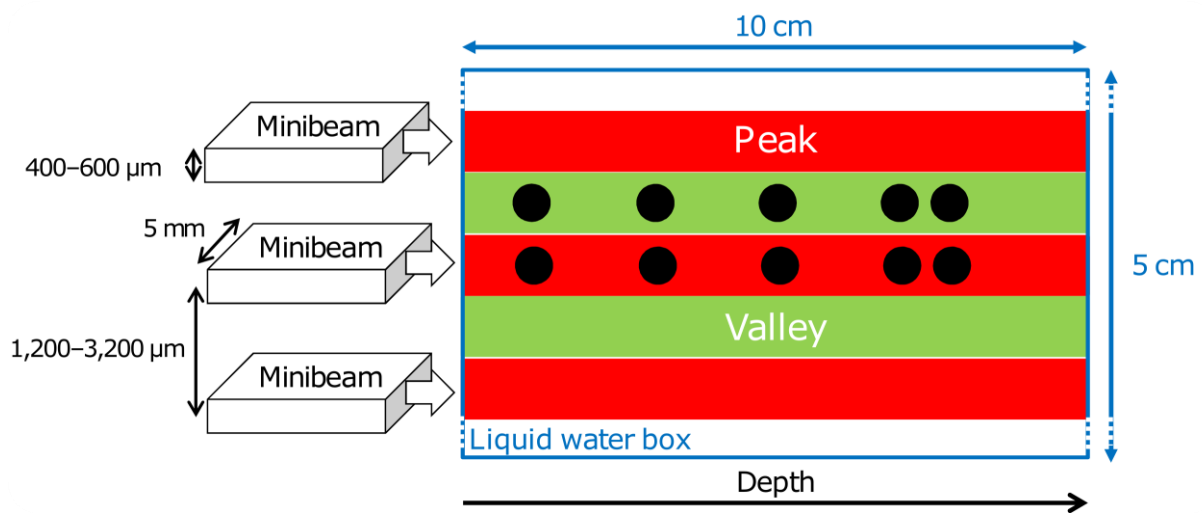
126 In the present study, for xMBRT, three minibeam of 600 $\mu\text{m} \times 5 \text{ mm}$ with a center-to-center distance
127 of 1,200 μm were simulated. The effective energy of the photon beam was 69 keV, based on the
128 photon energy spectrum of the SAARP facility. For the sake of simplification of this theoretical study,
129 time savings, and increase of statistics to reach the targets, we did not simulate the collimator. Instead,
130 we used rectangular sources to represent the minibeam at the position of the collimator exit, with no
131 divergence considered. This configuration approximated synchrotron xMBRT,⁴ for which a spatially
132 fractionated dose over the entire depth is expected.

133 Concerning pMBRT, minibeam of 400 $\mu\text{m} \times 5 \text{ mm}$ with a center-to-center distance of 3,200 μm were
134 simulated. An energy of 100 MeV was used for primary protons (Bragg peak position around 75 mm in
135 water), and a realistic beam divergence of 3 mrad was taken into account.^{14,32} The collimator was not

136 simulated. Instead, three minibeam at the position of the collimator exit were used. This configuration
 137 corresponded to what would have been obtained with a magnetic collimation of the beam.
 138 Based on previous theoretical studies,^{13,33} for eMBRT approach, the beam energy chosen for the
 139 primary electrons was 300 MeV. Three minibeam of 600 $\mu\text{m} \times 5\text{ mm}$ with a center-to-center distance
 140 of 1,800 μm were simulated. According to previous feasibility studies, beam divergence compatible
 141 with a beam size of 600 μm and with technically feasible beam optics on high-energy electron
 142 accelerators must be less than 0.2 mrad.^{31,33} Thus, beam divergence was not considered in the present
 143 study.

144 In electron and proton irradiation, beam size and beam spacing parameters were selected to obtain a
 145 highly spatially fractionated dose in the healthy tissue region (10–50 mm) and a quasi-homogeneous
 146 dose in the tumor region (approximately 70–75 mm) in order to favor tumor control. These irradiation
 147 configurations corresponded to that used in previous studies and represented the case of the deepest
 148 brain tumor.^{13,14,32}

149
 150 Spherical cells with a diameter of 20 μm , each containing a centered spherical nucleus of 10 μm in
 151 diameter, were placed in a $5 \times 5 \times 10\text{ cm}^3$ water phantom at different depths (1–75 mm) in the central
 152 minibeam path (peak) and in the next valley region, as illustrated in Figure 1. The cells were centered
 153 in the minibeam/valley both in lateral and vertical (2.5 mm from the edge of the minibeam) directions.



154
 155 **Figure 1. Scheme of the simulation configuration in the microdosimetry study. Three minibeam of 5 mm**
 156 **(vertical direction) are simulated, with a horizontal width of 400 μm for protons and 600 μm for electrons**
 157 **and photons. The minibeam are separated by 1,200 μm for photons, 1,800 μm for electrons and 3,200 μm**
 158 **for protons, and are transported in a 10 cm long water phantom. Spherical cells are positioned at depths of**
 159 **10, 30, 50, 70 and 75 mm in the central beam path (peak) and between two beams (valley).**

160
 161 To save computation time, only three minibeam have been simulated in all three irradiation
 162 modalities. In the case of electrons, the contribution in the central peak cells of the scattered dose due
 163 to an additional minibeam will amount 1 % of D_{max} at 5 cm depth and about 3% at the tumor position.
 164 Although the mean energy of the particles coming from the more extreme minibeam will be slightly
 165 higher, their number being much reduced, this will have a minimum impact in the mean energy. Similar
 166 findings will be observed in the three modalities. Being this a comparative evaluation between MBRT
 167 modalities, the inclusion of a higher number of minibeam will add unnecessary calculation time and
 168 not significantly change the conclusions of this work. In the microdosimetry study, the cell nuclei were
 169 filled only with water and the energy deposited as well as the number of events were scored. An

170 "event" must be understood here in the sense of a "Geant4 event", i.e. containing the history of a
171 primary particle tracked in the geometry as well as its possible secondary particles. Uncertainties on
172 the deposited energies per nucleus were calculated following the formula of Chetty *et al.*³⁴ for
173 multicore MC-based calculations.

174 In the nanodosimetry study, a detailed description of the sensitive target, the nucleosome (the first
175 DNA compaction level), was included to enable an evaluation of the RT-induced damage to cell nuclei.
176 The geometry of the nucleosome was extracted from an extended example of geant4
177 (*G4.10.1/example/extended/medical/dna/WholeNuclearDNA*). In brief, the nucleosome was
178 composed of a cylinder representing histone proteins wrapped by roughly two turns of DNA double
179 helix (~2 nm of diameter) containing 200 amino bases and a sugar phosphate corresponding region,³⁵
180 as shown in Figure 2. The construction of the sugar phosphate region is based on an association of
181 small spheres, forming a continuous volume for each strand. The nucleosomes were randomly
182 oriented in the nucleus with respect to the beam orientation. The two DNA strands were flagged
183 differently to calculate the type of breaks. The cell nucleus contained 29,925,000 nucleosomes,
184 corresponding roughly to 6 Giga base pairs (Gbp). Due to the huge memory required to simulate the
185 entire DNA of one cell in Geant4, with 24 Gigabytes of memory needed for each job, we used one-third
186 of the total DNA (roughly 2 Gbp) in our simulations. Because of the low probability of interaction with
187 the DNA when we simulated the whole three-minibeam source in the water phantom, we separated
188 these simulations into two parts. This is a commonly used method for multi-scale studies requiring
189 track-structure precision in small targets with realistic RT sources.³⁶ We previously verified that a one-
190 step simulation, i.e. transporting particles from a reduced source surface in the whole water volume
191 to the DNA, yields equivalent number of simple strand break (SSB) than the two-step method. The one-
192 step simulation requires 1000 times the number of primary particles to get the same statistical
193 uncertainty than with the two-step method, even with a simplified source. The method adopted in this
194 work was the following: 1) in a first step, we used the same geometry as that employed in the
195 microdosimetry study (Figure 1) to recover the energy spectrum of the particles (primary and
196 secondary) in square targets of $20 \times 20 \mu\text{m}^2$ placed $10 \mu\text{m}$ before each cell at all depths (10–75 mm)
197 and in both regions (peak and valley). 2) In a second step, we used these recorded energy spectra as
198 the source for the second simulation. Each source of $20 \times 20 \mu\text{m}^2$ was sent in a single cell in which the
199 detailed description of the DNA was included (Figure 2). The source was placed $10 \mu\text{m}$ before the cell
200 membrane and centered in a water box of $0.5 \times 0.5 \times 0.5 \text{ mm}^3$. The angular dispersion of the recorded
201 spectra was neglected, and all the particles were launched along the z-axis toward the cell. The particle
202 transport was performed using Livermore and standard hadronic physics of Geant4 outside the cells,
203 while Geant4-DNA physics was used inside the cells. The final number of DNA breaks was calculated
204 after normalizing by the initial number of particles sent in the three-minibeam source (first step
205 geometry) and by DNA Gbp. The calculation of DNA damage was considered as a counting following a
206 Poisson distribution. Uncertainty was therefore estimated from the square root of the obtained
207 number of breaks.

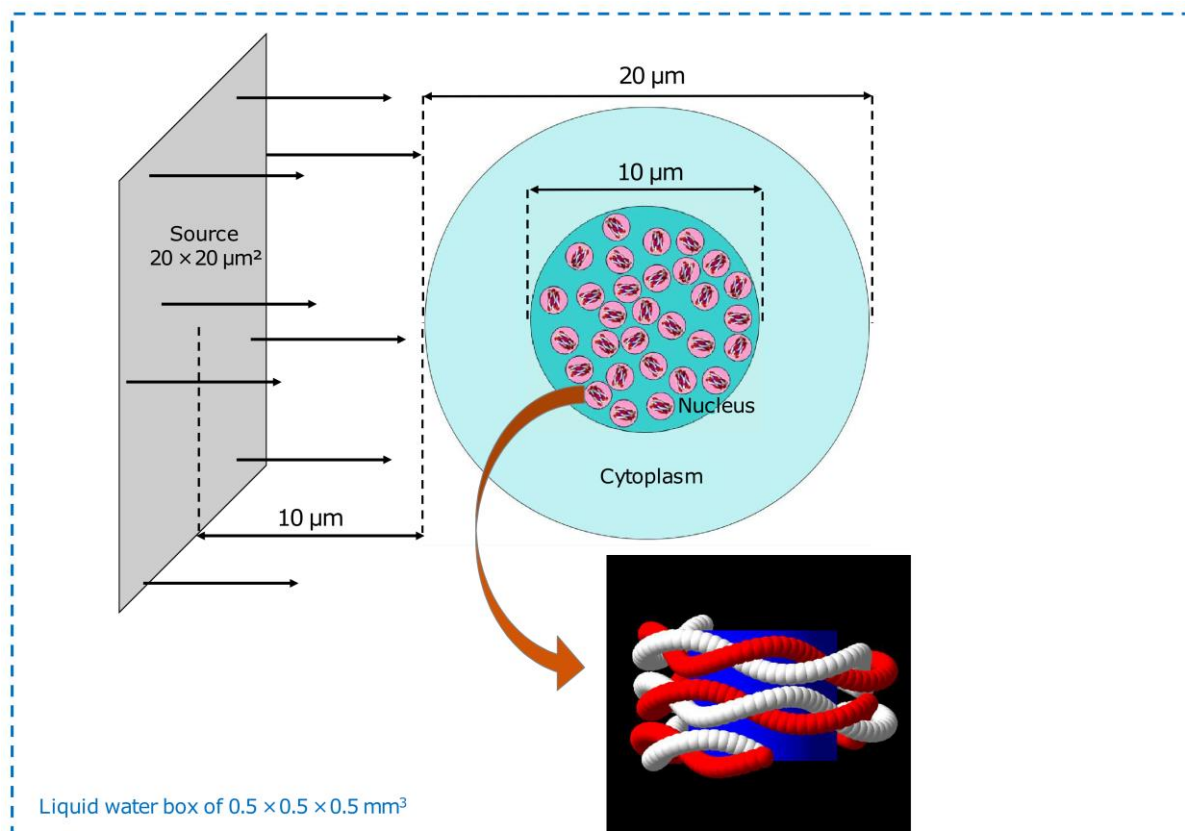


Figure 2. DNA geometry of the cell nucleus,³⁵ with a zoomed-up view of one nucleosome and the irradiation scheme used in the second step of the nanodosimetry simulations.

In the present study, a spherical nucleus of 10 μm in diameter corresponded to that of a neuronal cell, which defined the level of compaction of the modelled DNA. Using different sizes or shapes of nuclei would lead to different chromatin condensation and potentially different results in terms of DNA damage.

2.3. Analysis of DNA damage

The number of DNA breaks was assessed using a method developed at the Institute of Radioprotection and Nuclear Safety (IRSN) that combines the use of full DNA geometry and an adapted DBSCAN (Density-Based Spatial Clustering of Applications with Noise) algorithm. DBSCAN is a powerful method to reveal interaction points belonging to a same cluster and links between these points.^{35,37}

Thanks to the detailed DNA geometry introduced in the simulations, all the energy transfer points located in the region of interest (i.e., DNA) were selected. As mentioned in the previous section, each nucleosome contain two sugar phosphate continuous volumes not allowing the distinction between nucleotides. To differentiate whether the energy transfer points belonged to the same strand (SSB) or to opposite strands (double-strand break [DSB]), each volume has been marked. The impossibility of counting directly the number of base pairs or nucleotide for DNA damage determination impose the use of a clustering algorithm to assess DNA clustered damage. The energy transfer points located on the target region were analyzed and we used the adapted DBSCAN algorithm to obtain the energy deposition cluster that contributed to direct DNA damage. Although it is true that some other codes like PARTRAC³⁸ allows for a molecular precision, being the main purpose of this paper to relatively compare three new modalities of MBRT under the same conditions, Geant4-DNA is an adequate tool

233 that allows us to consider particle transport in a whole nucleus DNA. In this study, we simulated only
234 the physical stage of the interactions (i.e., the direct effect of ionizing radiation). Thus, the
235 quantification of DNA damage revealed by the clustering algorithm represented only potential clusters
236 of SSBs or DSBs. To identify these clusters, three parameters were defined:

- 237 • The minimum number of energy transfer points composing a cluster was two.
- 238 • The maximal distance between two energy transfer points composing a cluster was 3.2 nm, as
239 it is the distance between 10 base pairs, ensuring that the resulting clusters represented
240 potential DSBs.^{39–41}
- 241 • The minimal energy contained in a cluster was 10 eV or the minimal energy of each energy
242 transfer point was 5 eV.

243 From these considerations, three types of damage were distinguished:

- 244 • An isolated SSB (SSBis): energy transfer point located more than 3.2 nm from another point.
- 245 • A complex SSB (SSBcplx): two or more energy transfer points located on the same strand and
246 separated by less than 3.2 nm.
- 247 • A DSB: two or more energy transfer points located on two strands and separated by less than
248 3.2 nm.

249 Although DSBs play a key role in inducing cell death, we scored all DNA damage candidates. We have
250 chosen to present separately isolated SSBs to clustered SSBs (corresponding roughly to the "SSB+"
251 damage category in the DNA break classification proposed by Nikjoo et al.³⁹) as more energy is
252 deposited locally on a clustered damage, which is potentially more difficult to repair. As in our
253 geometry two energy transfer points, in a same strand, could be located in a same nucleotide and
254 counted as a SSBcplx, a slight overestimation of the number of SSBcplx could be expected.
255

256 **3. Results**

257 *3.1. Microdosimetry study*

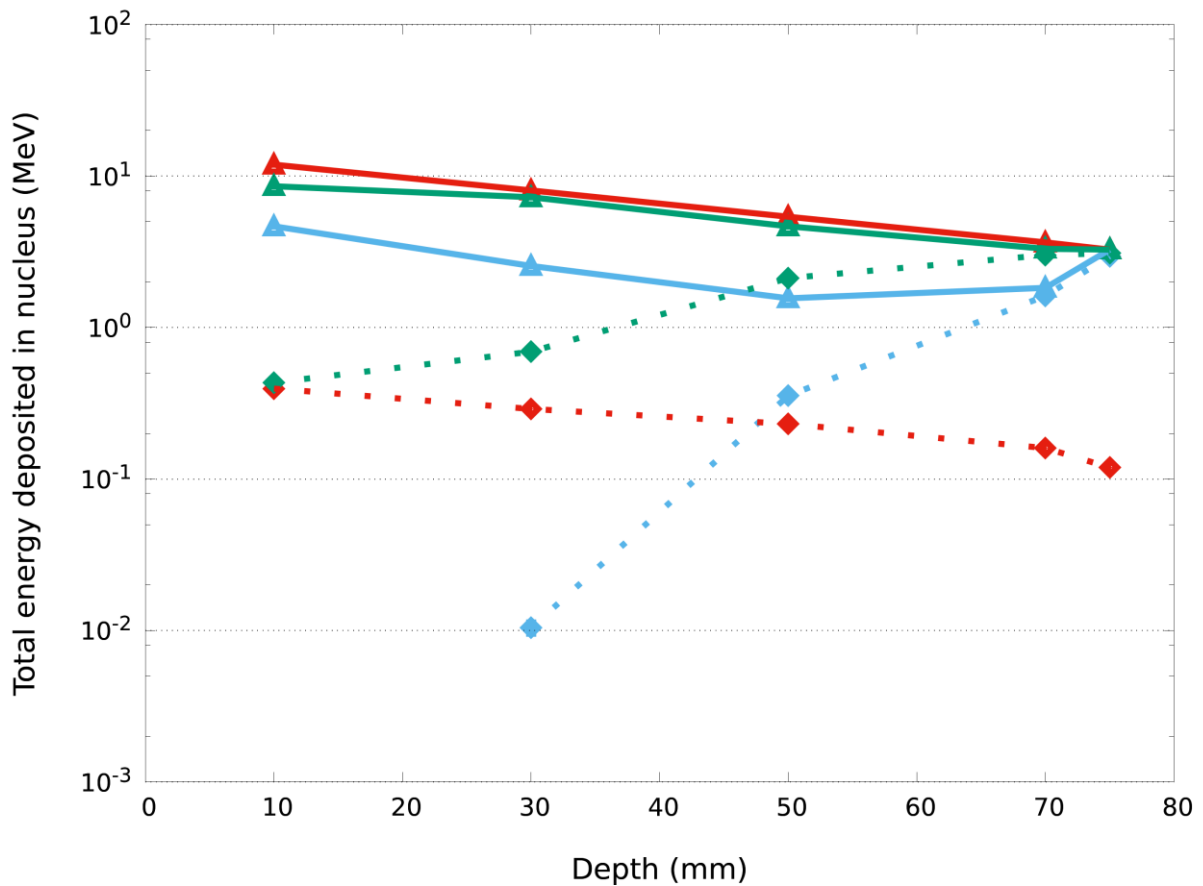
258 Three parameters were studied: the total energy deposited in cell nuclei, the energy deposited in cell
259 nuclei by event (i.e., a particle, primary or secondary, that interacted at least once with the cell
260 nucleus), and the interaction probability in cell nuclei. For all configurations, the PVDR was calculated.
261 Global statistical uncertainties of < 1% in peak cell nuclei and of < 2% in most valley cell nuclei were
262 achieved. Only the point at 30 mm in valley for pMBRT presented a higher uncertainty of 8%.

263

264 *3.1.1. Energy deposited in cell nuclei*

265 Figure 3 shows the evolution of the total energy deposited in cell nuclei as a function of the depth in
266 peak and valley regions for xMBRT, pMBRT and eMBRT. To compare the three modalities, the results
267 were normalized to obtain the same absorbed dose (1 Gy) in the central peak cell nucleus at the tumor
268 depth of 75 mm.

269



270
271
272
273
274

Figure 3. Total energy deposited in cell nuclei located in peak and valley regions for xMBRT (red), pMBRT (blue), and eMBRT (green) normalized at a depth of 75 mm in the central peak. The triangle symbols and solid lines depict the peak region, and the diamond symbols and dotted lines denote the valley region.

275
276
277
278
279

Table 1 shows the calculated PVDR for xMBRT, pMBRT and eMBRT. The PVDR is an important dosimetric parameter in spatially fractionated radiotherapy, as previous research showed that it was related to the dose tolerance of normal tissues.²² In the present study case, high PVDR values obtained at shallow depths suggested that normal tissue sparing could be expected.

280
281

Table 1. Peak-to-valley dose ratio (PVDR) values as a function of depth in water for xMBRT, pMBRT, and eMBRT modalities.

Depth (mm)	PVDR		
	xMBRT	pMBRT	eMBRT
10	30.0 ± 0.2		19.8 ± 0.3
30	27.7 ± 0.2	246 ± 22	10.5 ± 0.1
50	23.3 ± 0.2	4.4 ± 0.1	2.20 ± 0.02
70	22.8 ± 0.2	1.13 ± 0.02	1.10 ± 0.01
75	27.5 ± 0.3	1.11 ± 0.02	1.06 ± 0.01

282
283

284
285
286

The results obtained for MBRT revealed an exponential decrease in the energy deposited with depth and this decrease was similar in peak and valley regions. As divergence of the minibeam source was not considered in this study, the observed behavior was similar to that of synchrotron minibeam

287 profiles, where the PVDR remained relatively constant with depth due to the very low energy of the
288 secondary particles.⁴

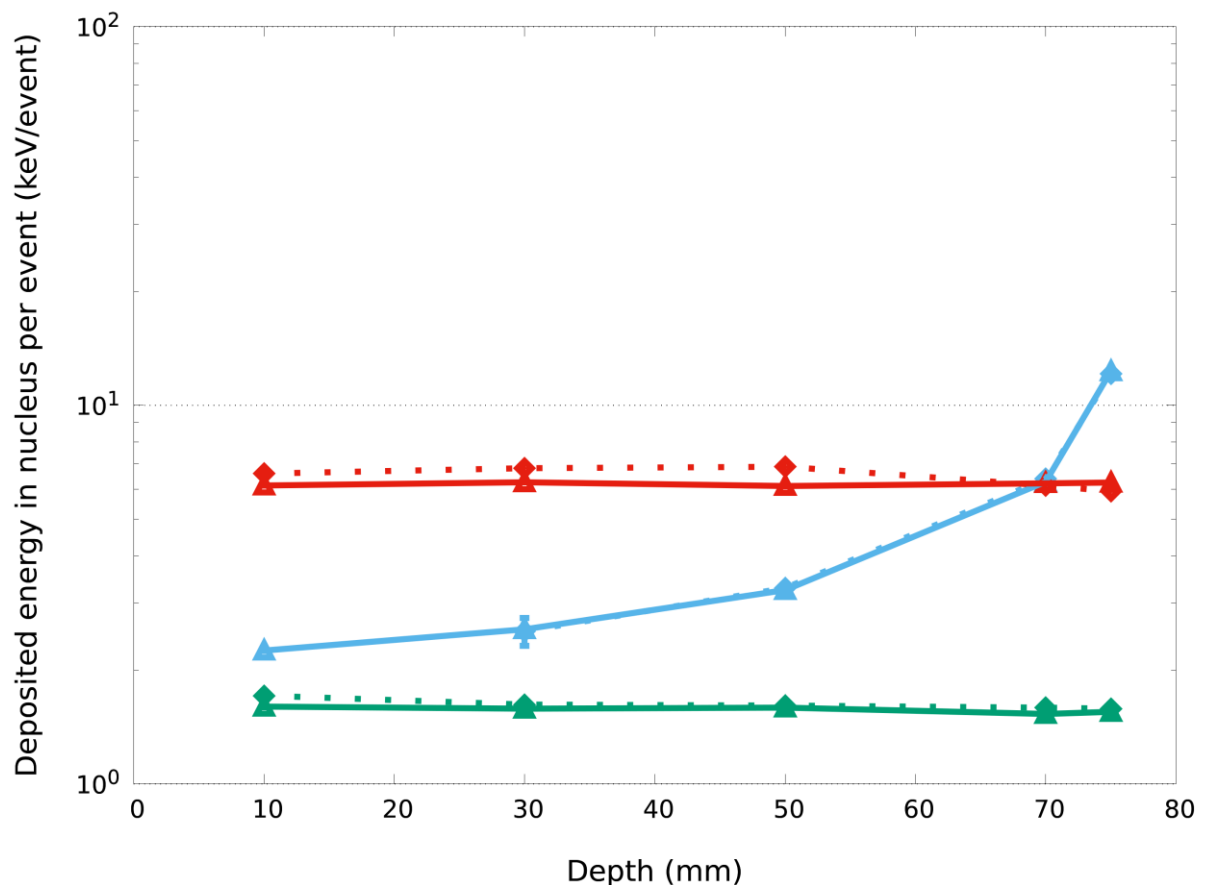
289 Regarding eMBRT, the energy deposition in the peak region followed the same trends as observed with
290 xMBRT. The decrease was mainly due to the very small beam sizes used and their rapid lateral
291 spreading with depth. In the case of minibeam, 300 MeV electrons exhibit substantial lateral
292 scattering at a deep depth. Thus, a small beam size induces electronic disequilibrium in the central
293 minibeam axis. The latter has a significant impact on energy deposition in depth, despite the very high
294 energy used, as shown in previous studies.¹³ In the present study, the small beam size in eMBRT
295 compensated for the high energy of the electrons, and this compensation was sufficient to cause a
296 depth profile decrease as steep as for the 69 keV photon beam. The energy deposition in the valley
297 was the highest among the three modalities compared at all depths.

298
299 The results obtained for pMBRT showed that the lowest amount of energy was deposited in cell nuclei
300 both in the peak and valley regions, which should favor tissue sparing. The energy deposited in valley
301 cells was one order of magnitude smaller than in the case of xMBRT or eMBRT before a depth of
302 50 mm. As for eMBRT, the very small beam size used impacted deeply the minibeam depth-profile, as
303 shown in previous studies.^{13,14} However, lateral spreading was widely compensated by the Bragg peak
304 (an increase in the track density) at the tumor location. There was a significant increase of deposited
305 energy in nuclei in the peak region, with an associated PVDR close to 1 at depths of 70–75 mm. Using
306 this pMBRT configuration, high tolerance to radiation can be expected in healthy tissue, with a
307 favorable effect on tumor control.

308

309 3.1.2. *Energy deposited in cell nuclei per event*

310 Figure 4 reports the evolution of energy deposited in cell nuclei per event as a function of depth for
311 the three modalities. Here, an event corresponds to the Geant4-event term, i.e. a primary particle and
312 the possible secondary particles that it has produced. The event is only counted once when the primary
313 or its secondary particles have interacted one time or more in the nucleus with an associated energy
314 deposited in the volume. The final observable is the mean energy deposited in the cell nucleus per
315 event having produced at least one interaction in the nucleus. This observable reflected the track-
316 structure behavior of each irradiation modality at the micrometric scale.

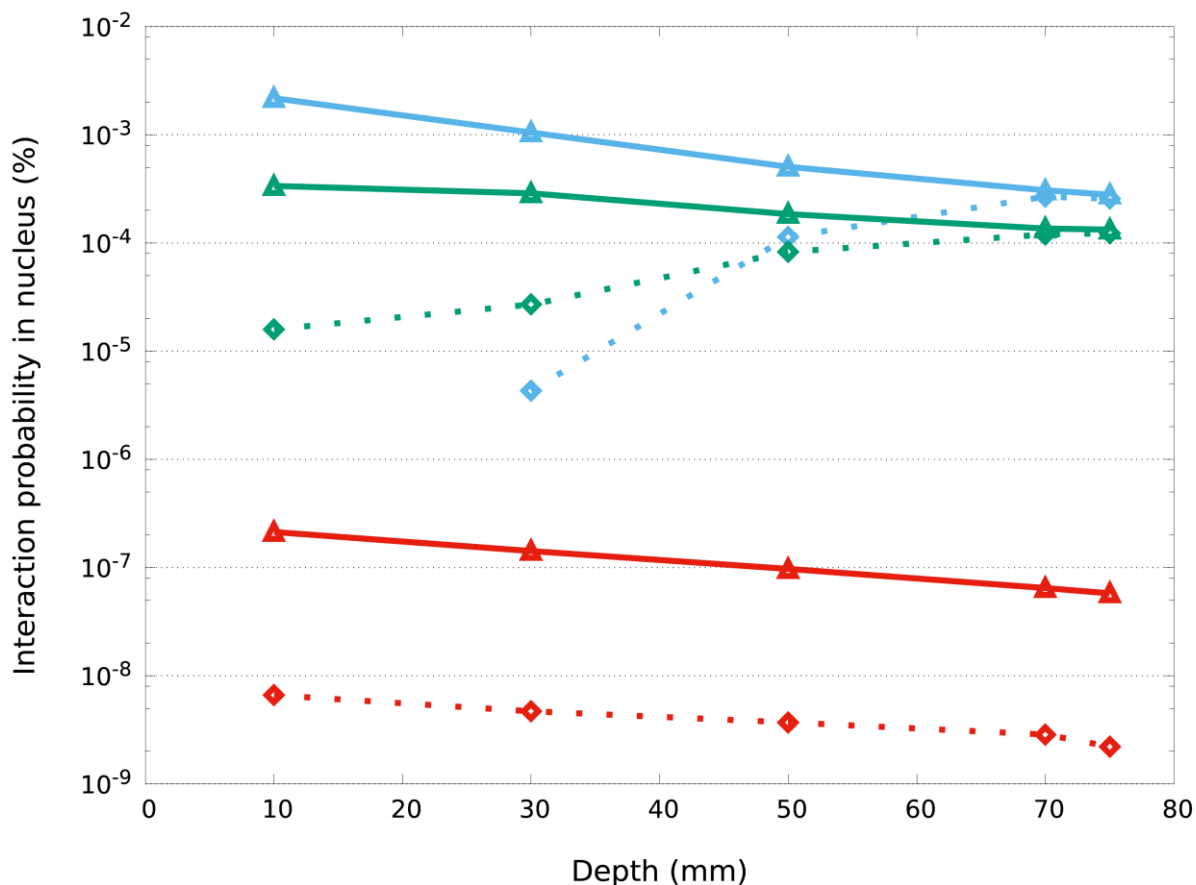


317
 318 **Figure 4. Energy deposited per event in cell nuclei for xMBRT (red), pMBRT (blue) and eMBRT (green). The**
 319 **triangle symbols and solid lines depict the peak region, and the diamond symbols and dotted lines denote**
 320 **the valley region.**
 321

322 For both xMBRT and eMBRT, no dependence with the depth or differences between peak and valley
 323 regions were observed. This finding can be explained by the energy spectrum, which does not change
 324 significantly in accordance with depth or region for these beam types. The values for photons were
 325 four times higher than those of VHEEs. In contrast, for pMBRT, the profile of energy deposited per
 326 event increased as a function of depth, reaching a maximum value at the Bragg peak position (five
 327 times higher than at the entrance point) both in peak and valley regions. Such an increase,
 328 accompanied by a significant increase in the average energy deposited in the nucleus (Figure 3),
 329 suggested that an event occurring in the tumor region is potentially more aggressive at the micrometric
 330 level than one at the entrance (healthy tissue region).
 331

332 3.1.3. Interaction probability

333 Figure 5 shows the interaction probability (i.e., the number of events interacting with the cell nucleus
 334 per primary particle) as a function of the depth for the three modalities. Both peak and valley regions
 335 were assessed.
 336



337
 338 **Figure 5. The interaction probability in cell nuclei for xMBRT (red), pMBRT (blue) and eMBRT (green). The**
 339 **triangle symbols and solid lines depict the peak region, and the diamond symbols and dotted lines denote**
 340 **the valley region.**
 341

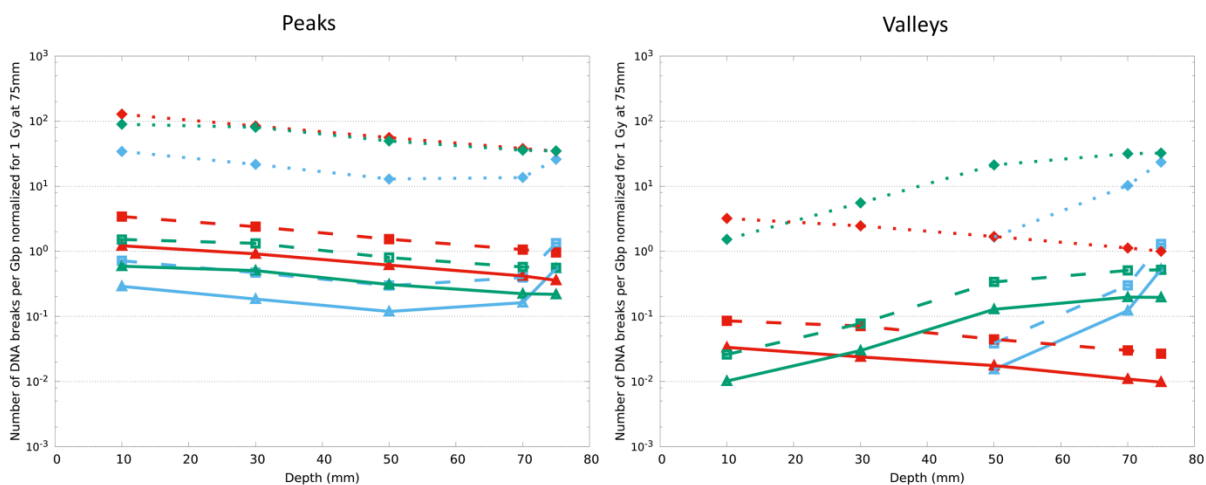
342 The expected exponential decrease in the interaction probability for photons was around 20 times
 343 higher in peak than in valley regions. Moreover, VHEEs and protons were much likely than photons
 344 were to interact with a targeted nucleus (around three orders of magnitude). This was due to their
 345 higher ionization density along their track. The differences in peak cells between eMBRT and pMBRT
 346 were also partly due to the geometric difference of beam size: 400 μm for protons versus 600 μm for
 347 electrons. The trend of the interaction probability as a function of depth followed that observed for
 348 energy deposition in both peak and valley regions (Figure 3). However, the number of events was not
 349 related to the increase of energy deposition observed in the Bragg peak in the peak region (Figure 3).
 350 This finding was mainly due to a decrease in the mean free path of the secondary particles, which
 351 delivered all their energy inside the cell nucleus. This phenomenon, highlighted by the energy
 352 deposited per event (Figure 4), was clearly due to the intrinsic properties of ion beams versus those of
 353 photon and electron beams.

354 3.2. Nanodosimetry study

356 We simulated the number and complexity of SSBs (isolated and clustered) and DSBs induced by direct
 357 interactions in cell nuclei for xMBRT, eMBRT and pMBRT. For pMBRT, in common with the findings of
 358 the microdosimetric study (Section 3.1), very little energy was deposited in the valley cell nuclei in the
 359 first 30 mm. Thus, DNA damage was calculated only from a depth of 50 mm in the valley region. The
 360 calculated uncertainties on the number of SSBs were < 0.5% for all modalities and $\leq 1\%$ on SSBcplx

361 and DSBs for both pMBRT and eMBRT. Using xMBRT, the uncertainties were 3% and 5% for SSBcplx
 362 and DSBs, respectively.

363 Figure 6 shows a comparison of the DNA damage among the three modalities normalized by the target
 364 dose (1 Gy peak dose at the tumor location, depth of 75 mm).
 365



366 **Figure 6. DNA damage (isolated SSBs, clustered SSBs and DSBs)/Gbp normalized for 1 Gy at 75 mm for**
 367 **xMBRT (red), pMBRT (blue), and eMBRT (green) in the peak (left) and valley (right) regions as a function of**
 368 **the depth. The triangle symbols and solid lines denote DSBs, the square symbols and dashed lines denote**
 369 **SSBcplx, and the diamond symbols and dotted lines denote SSBis.**

371 Irrespective of the irradiation modality, most of the DNA damage consisted of isolated SSBs (93–98%).
 372 Complex SSBs and DSBs accounted for only 1.5–5% and 0.5–2% of DNA damage, respectively. This
 373 finding can be explained by the very small volume of DNA molecules (0.20%) to that of the total volume
 374 of the cell nucleus. Hence, the probability of having energy transfer points close enough to form DSBs
 375 was weaker than the probability of having isolated energy transfer points.
 376

377 As a complement to Figure 6, Table 2 reports the total number of direct DNA breaks as a function of
 378 depth for pMBRT, eMBRT and xMBRT in peak and valley regions.

379 **Table 2. Total amount of direct DNA damage/Gbp normalized for 1 Gy at 75 mm, in the peak (left) and valley**
 380 **(right) regions for pMBRT, eMBRT and xMBRT modalities.**

Total DNA breaks per Gbp, normalized for 1 Gy at 75 mm		
Depth (mm)	pMBRT-peak	pMBRT-valley
10	35.37 ± 0.04	
30	22.31 ± 0.02	
50	13.35 ± 0.01	1.713 ± 0.001
70	14.18 ± 0.01	10.690 ± 0.006
75	27.80 ± 0.01	25.355 ± 0.009
Depth (mm)	eMBRT-peak	eMBRT-valley
10	91.77 ± 0.08	1.569 ± 0.001
30	82.55 ± 0.07	5.674 ± 0.004
50	50.76 ± 0.04	21.71 ± 0.02
70	36.59 ± 0.03	32.40 ± 0.03
75	35.66 ± 0.03	32.99 ± 0.03
Depth (mm)	xMBRT-peak	xMBRT-valley
10	132.6 ± 0.7	3.32 ± 0.02
30	87.7 ± 0.4	2.56 ± 0.01
50	58.2 ± 0.3	1.75 ± 0.01
70	39.4 ± 0.2	1.17 ± 0.01
75	36.0 ± 0.2	1.04 ± 0.01

381
382

383 These results indicated that, compared to eMBRT or xMBRT, in the peak, the quantity of DNA damage
384 events was lower in the case of pMBRT between 10 and 70 mm, which might favor sparing of healthy
385 tissue. Moreover, due to an increase in track density in the tumor location at a depth of 75 mm, pMBRT
386 resulted in the highest number of complex DNA damage events, such as DSBs, which are the most
387 critical type of DNA lesion (Figure 6). This finding suggests that pMBRT could be expected to result in
388 more lethal lesions at the tumor position than eMBRT or xMBRT. The number of complex DNA breaks
389 obtained in the valley region was negligible or very low before 50 mm. However, this number increased
390 with depth, reaching an equivalent level to that of the peak obtained at 75 mm, highlighting the
391 homogenous irradiation effect of pMBRT at the tumor site. These observations were correlated with
392 the theoretical results obtained in the microdosimetric study, in which higher energy was deposited
393 per event at 75 mm (Figure 4).

394 In the peak region of xMBRT and eMBRT, a similar steady decline in the total number of DNA damage
395 events was observed with depth, in accordance with the observations of the interaction probability
396 and total energy deposited in cell nuclei reported above (Section 3.1). The number of clustered SSBs
397 and DSBs obtained using xMBRT was slightly greater than that obtained using eMBRT.

398 In the valley region, the total number of DNA damage events caused by eMBRT increased with depth
399 until reaching a value similar to that of the peak obtained at 75 mm. In contrast, the total number of
400 xMBRT-induced DNA damage events continued to decrease with depth, with a steadily lower amount
401 compared to the peak by a factor of around 35. The difference factor in complex DNA breaks (SSBcplx
402 and DSBs) between the peak and the valley was around 60 after eMBRT at a depth of 10 mm, and
403 became equivalent to that caused by xMBRT at 30 mm. In accordance with the microdosimetric study,
404 this result suggested that low damage can be expected on entrance tissues with eMBRT. At a depth of

405 50 mm, the number of complex DNA breaks in the valley region was higher using eMBRT by an order
406 of magnitude as compared with those obtained using xMBRT and pMBRT. In the tumor region (70–75
407 mm), this number increased using eMBRT due to lateral spreading of the electron beam with depth,
408 confirming the homogeneous damaging effect of charged beams on peaks and valleys at the nanoscale.
409 The maximum number of DSBs occurred at a depth of 75 mm using both pMBRT and eMBRT, showing
410 that important cell death can be expected in the tumor region, even in the valley's axis.

411 Although the proportions of complex DNA breaks (i.e., SSBcplx and DSBs) remained constant at all
412 depths for xMBRT (approximately 2.5% and 1%, respectively) and eMBRT (approximately 1.6 and 0.6%,
413 respectively), the proportion of SSBcplx and DSBs increased and reached maximum values of 5% and
414 2% at 75 mm for pMBRT, respectively. The latter finding was the result of an increase in radiation linear
415 energy transfer (LET) of protons with depth.

416 In terms of complexity (i.e., the number of energy transfer points composing clusters), there was an
417 exponential decrease in the number of DNA breaks with the cluster size, irrespective of the irradiation
418 modality. In the case of pMBRT and eMBRT, about 90% of SSBcplx and 73% of DSBs were composed of
419 two or three energy transfer points, both in the peak and valley regions. For these two modalities, DSB
420 clusters containing as many as 15 energy transfer points were detected, although at a very small
421 frequency. For xMBRT, the clusters were slightly less complex, with 92% of SSBcplx and 76% of DSBs
422 composed of two or three energy transfer points, and DSB clusters that did not exceed 10 energy
423 transfer points. In terms of the proportion of complexity level, no significant differences were found
424 among peak and valley regions or depth for all modalities. However, the maximal number of damage
425 events for a given complexity was found for pMBRT at the tumor depth (75 mm).

426

427 **4. Discussion**

428 This study compared micro- and nanodosimetric characteristics of three innovative types of spatially
429 fractionated RT: photon, electron and proton minibeam radiation therapy. xMBRT and pMBRT
430 approaches have been the subject of several dosimetric^{14,32} and biological studies,^{5–8,42} and these have
431 demonstrated very promising results as a treatment for radioresistant tumors. However, the
432 underlying mechanisms remain unclear. In addition, eMBRT using very high-energy electrons has never
433 been studied experimentally, although theoretical studies pointed to potentially interesting properties
434 in terms of normal tissue sparing.^{13,33} This is the first multiscale MC study mimicking realistic conditions
435 of minibeam treatments, and the results allow to deepen understanding of the physical mechanisms
436 involved in xMBRT approaches down to the DNA level. The latter was made possible by the precision
437 of Geant4-DNA^{26–29} code, detailed geometry of human neuronal DNA, and use of the adapted
438 clustering DBSCAN algorithm.^{35,37}

439

440 Concerning a depth of 10–50 mm representative of healthy tissue, the energy deposition in cell nuclei
441 located in the valley region was very low, resulting in high PVDR values (Section 3.1). In addition, the
442 number of complex direct DNA damage events in the valley region was at least one order of magnitude
443 lower than in the peak region (Section 3.2). These results suggested a potential gain in normal tissue
444 sparing for all the modalities studied. Among the three modalities, pMBRT was associated with the
445 lowest amounts of energy deposition and DNA breaks, both in peak and valley cell nuclei, when the
446 results were normalized to a target dose of 1 Gy at 75 mm depth.

447 Regarding the tumor location (70–75 mm), both eMBRT and pMBRT appeared to favor tumor control
448 by delivering a quasi-homogeneous energy distribution at the depth of the tumor. Using xMBRT, the
449 proportion of energy deposition and direct DNA breaks between peak and valley regions remained
450 relatively constant from entrance to tumor depth.

451

452 The results of the nanodosimetry study showed that all modalities caused a significant number of
453 direct complex DNA breaks, such as DSBs and clustered SSBs, in the tumor region. We focused
454 attention on complex DNA breaks because they are the most critical lesion to cause cell death,
455 especially DSBs.^{43,44} Photons have the lowest probability of interacting with targets as small as DNA.
456 Hence, at least 10,000 additional primary particles are needed to reach similar DNA break values to
457 those of charged beams. In the present study, the proportion of complex SSBs and DSBs at the tumor
458 site (75 mm) using pMBRT was much higher than that obtained using eMBRT or xMBRT in both peak
459 and valley regions (up to 7% of clustered DNA damage versus 3% for electrons and photons). In
460 addition, clusters composed of up to 15 energy transfer points and separated by less than 3.2 nm were
461 obtained using eMBRT and pMBRT, whereas clusters composed of up to 10 energy transfer points were
462 found for xMBRT.

463

464 Finally, pMBRT may be superior to xMBRT and eMBRT in terms of radioresistant tumor control, as it
465 was associated with a higher number of complex DNA breaks and higher energy deposition, and energy
466 per event, at the cell nucleus level when scored at the tumor depth. In addition, pMBRT showed the
467 lowest energy deposition and the lowest number of DNA lesions in healthy tissue.

468 xMBRT may be a promising treatment modality in cases where the advantages of spatial fractionation
469 are required at all depths. In such cases, to decrease PVDR values and obtain a quasi-homogenous
470 dose distribution in the tumor, an orthogonal array of interlaced minibeam irradiation must be used.⁶
471 In relation to eMBRT, this modality may be useful for skin and superficial tissue protection. It also offers
472 the advantage of a homogeneous dose to favor tumor control at a potentially lower cost than proton
473 beams. When submillimetric beams are used to treat deep tumors, the use of several beam incidences
474 can additionally increase the dose deposition. However, the gain expected for normal tissues located
475 close to the tumor would be very limited as compared with that obtained using pMBRT.

476 Thus, depending on the tumor location, normal tissue sparing, and nearby organs at risk, each
477 configuration could be used (pMBRT, eMBRT or xMBRT), potentially enhancing conventional treatment
478 for cancers not benefiting currently from a satisfactory curative solution. These results pave the way
479 for additional studies on the effectiveness of MBRT modalities for the treatment of radioresistant
480 tumors or pediatric cancers, as the treatment doses could be increased while limiting damage to
481 healthy tissues surrounding a tumor.

482 As a proof of concept, we considered a tumor located in the center of the brain, i.e., a deeply
483 embedded brain tumor with a poor prognosis due to the potential high doses deposited in the
484 surrounding normal tissue. Our results do not need to be restricted to brain location and could be
485 extrapolated for any tumor located at such depth. However, we remind the reader that a modification
486 of the size or the shape of the cell nucleus may lead to a different DNA condensation and potentially
487 to different DNA damage results. For other tumor depths, as PVDR values and the proportion of DNA
488 breaks in healthy tissue and tumor may vary, different beam sizes and center-to-center distances may
489 be selected to optimize the treatment, depending on the tumor site. In the present study, to reduce
490 the computation time while ensuring the nanometric precision needed, the simulations were

491 performed using only three minibeam instead of a full array of minibeam as would be the case in a
492 realistic treatment to cover macroscopic targets. Although non-negligible for VHEE beams, the missing
493 contribution due to long-range secondary particles does not alter the conclusions of the present study
494 in terms of relative effectiveness of the different MBRT modalities.

495 In the last decades, several cell nuclei models containing DNA geometry have been implemented in
496 MC simulations to quantify DNA damage and to aid understanding of their biological effects. Different
497 MC codes (e.g., KURBUC or PARTRAC), geometry models, DNA break quantification methods and, for
498 the most advanced codes, DNA repair processes have been used in calculations aiming of quantifying
499 DNA damage.^{28,38,45,46} In the present study, we simulated only the physical stage of the interactions
500 (i.e., the direct effect of ionizing radiation), as a result of which we did not calculate absolute numbers
501 of DNA breaks. Thus, our results cannot be directly compared to DNA break yields published in previous
502 MC studies.^{38,46} Moreover, most of these studies focused on charged particles (i.e., protons, alpha
503 particles and heavier ions) with specific LET and for which the sources were delivered directly to the
504 cell nucleus. In our calculations, we endeavored to closely simulate the real irradiation conditions in
505 minibeam therapies. The main objective of this study was to compare for the first time three promising
506 MBRT modalities at radiobiological scales. An additional original contribution was to evaluate the
507 situation of VHEE beams in comparison to photon and proton beams at such scales. To the best of our
508 knowledge, this is the first micro- and nanodosimetry study on MBRT. In addition, no *in vitro* or *in vivo*
509 experiments have compared these three modalities. For these reasons, it is not possible to compare
510 our results with previous numerical studies or experiments. Moreover, although it holds true that
511 Geant4-DNA does not transport heavy ions produced with energies lower than 0.5 MeV/u in the case
512 of VHEE, our calculations demonstrated that their production rate is four order of magnitude smaller
513 than that of secondary electrons and photons. Thus, this limitation should not alter the conclusions of
514 this work.

515 To go further, it would be interesting to simulate indirect effects of ionizing radiation, as a large amount
516 of DNA damage is caused by radiolytic products resulting from water radiolysis after irradiation.^{47,48}
517 Such researches would improve the realism of our damage estimations to allow comparisons to other
518 MC simulation results or biological data. Geant4-DNA can already be used to study the production and
519 transportation of chemical species, although only in liquid water.⁴⁹ It will be interesting to perform
520 simulations of the physico-chemical and chemical stages of radiation in detailed DNA geometries when
521 the processes will be available for the public in Geant4.^{49,50} Finally, systematic *in vitro* and *in vivo*
522 experimental measurements would be required to validate the therapeutic benefit of these promising
523 MBRT modalities.

524

525 **5. Conclusion**

526 This work compared the micro- and nanodosimetric characteristics of xMBRT, eMBRT, and pMBRT,
527 three innovative RT approaches based on spatial fractionation and the use of submillimetric irradiation
528 beams. The MC results presented herein provide additional micro- and nanometric arguments in favor
529 of developing these new MBRT modalities for cancer treatment. Among the modalities assessed in the
530 present study, pMBRT showed the highest potential in terms of normal tissue preservation. It was also
531 the most aggressive treatment in the tumor region (located at 75 mm in this study). Future studies will
532 focus on performing systematic radiobiology experiments to explore the impact of these promising
533 MBRT modalities on DNA damage *in vitro* and to validate their therapeutic benefit *in vivo*.

534

535 **Acknowledgments**

536 The authors acknowledge PRACE for awarding access to MareNostrum computational cluster at BSC
537 (Spain) under the grant agreement number 2016153507. This work was also granted access to the
538 HPC resources of CINES under the allocation 2018-A0040307312 made by GENCI.

539

540 **Conflicts of interest**

541 All the authors declare that they have no conflict of interest in relation to the research in the submitted
542 manuscript.

543 **References**

- 544 1. Favaudon V, Caplier L, Monceau V, et al. Ultrahigh dose-rate FLASH irradiation
545 increases the differential response between normal and tumor tissue in mice. *Sci*
546 *Transl Med.* 2014;6(245):245ra93. doi:10.1126/scitranslmed.3008973
- 547 2. Dilmanian FA, Zhong Z, Bacarian T, et al. Interlaced x-ray microplanar beams: a
548 radiosurgery approach with clinical potential. *Proc Natl Acad Sci U S A.*
549 2006;103(25):9709-9714. doi:10.1073/pnas.0603567103
- 550 3. Deman P, Vautrin M, Edouard M, et al. Monochromatic minibeam radiotherapy:
551 From healthy tissue-sparing effect studies toward first experimental glioma bearing
552 rats therapy. *Int J Radiat Oncol Biol Phys.* 2012;82(4):e693-e700.
553 doi:10.1016/j.ijrobp.2011.09.013
- 554 4. Prezado Y, Deman P, Varlet P, et al. Tolerance to Dose Escalation in Minibeam
555 Radiation Therapy Applied to Normal Rat Brain: Long-Term Clinical, Radiological and
556 Histopathological Analysis. *Radiat Res.* 2015;184(3):314-321. doi:10.1667/RR14018.1
- 557 5. Prezado Y, Dos Santos M, Gonzalez W, et al. Transfer of Minibeam Radiation Therapy
558 into a cost-effective equipment for radiobiological studies: a proof of concept. *Sci Rep.*
559 2017;7(1):17295. doi:10.1038/s41598-017-17543-3
- 560 6. Prezado Y, Sarun S, Gil S, Deman P, Bouchet A, Le Duc G. Increase of lifespan for
561 glioma-bearing rats by using minibeam radiation therapy. *J Synchrotron Radiat.*
562 2012;19(1):60-65. doi:10.1107/S0909049511047042
- 563 7. Prezado Y, Jouvion G, Hardy D, et al. Proton minibeam radiation therapy spares
564 normal rat brain: Long-Term Clinical, Radiological and Histopathological Analysis. *Sci*
565 *Rep.* 2017;7(1). doi:10.1038/s41598-017-14786-y
- 566 8. Prezado Y, Jouvion G, Patriarca A, et al. Proton minibeam radiation therapy widens
567 the therapeutic index for high-grade gliomas. *Sci Rep.* 2018;8(1):16479.
568 doi:10.1038/s41598-018-34796-8
- 569 9. Pouzoulet F. Platform of Experimental Radiotherapy. [http://www.institut-](http://www.institut-curie.org/research/experimental-radiotherapy-platformradexp)
570 [curie.org/research/experimental-radiotherapy-platformradexp](http://www.institut-curie.org/research/experimental-radiotherapy-platformradexp). Published 2019.
- 571 10. Prezado Y, Fois GR. Proton-minibeam radiation therapy: A proof of concept. *Med*
572 *Phys.* 2013;40(3):031712. doi:10.1118/1.4791648
- 573 11. Peucelle C, Martínez-Rovira I, Prezado Y. Spatial fractionation of the dose using neon
574 and heavier ions: A Monte Carlo study. *Med Phys.* 2015;42(10):5928-5936.
575 doi:10.1118/1.4930960
- 576 12. González W, Peucelle C, Prezado Y. Theoretical dosimetric evaluation of carbon and
577 oxygen minibeam radiation therapy. *Med Phys.* 2017;44(5):1921-1929.
578 doi:10.1002/mp.12175
- 579 13. Martínez-Rovira I, Fois G, Prezado Y. Dosimetric evaluation of new approaches in GRID
580 therapy using nonconventional radiation sources. *Med Phys.* 2015;42(2):685-693.

- 581 doi:10.1118/1.4905042
- 582 14. Peucelle C, Nauraye C, Patriarca A, et al. Proton minibeam radiation therapy:
583 Experimental dosimetry evaluation. *Med Phys*. 2015;42(12):7108-7113.
584 doi:10.1118/1.4935868
- 585 15. De Marzi L, Patriarca A, Nauraye C, et al. Implementation of planar proton minibeam
586 radiation therapy using a pencil beam scanning system: A proof of concept study. *Med*
587 *Phys*. 2018;45(11):5305-5316. doi:10.1002/mp.13209
- 588 16. Paganetti H, Niemierko A, Ancukiewicz M, et al. Relative biological effectiveness (RBE)
589 values for proton beam therapy. *Int J Radiat Oncol Biol Phys*. 2002;53(2):407-421.
- 590 17. DesRosiers C, Moskvina V, Bielajew F, Papiez L. 150-250 meV electron beams in
591 radiation therapy. *Phys Med Biol*. 2000;45(7):1781-1805. doi:10.1088/0031-
592 9155/45/7/306
- 593 18. Schüler E, Eriksson K, Hynning E, et al. Very high-energy electron (VHEE) beams in
594 radiation therapy; Treatment plan comparison between VHEE, VMAT, and PPBS. *Med*
595 *Phys*. 2017;44(6):2544-2555. doi:10.1002/mp.12233
- 596 19. Curtis HJ. The Use of a Deuteron Microbeam for Simulating the Biological Effects of
597 Heavy Cosmic-Ray Particles. *Radiat Res Suppl*. 1967;7:250. doi:10.2307/3583718
- 598 20. Lawrence YR, Li XA, el Naqa I, et al. Radiation Dose–Volume Effects in the Brain. *Int J*
599 *Radiat Oncol*. 2010;76(3):S20-S27. doi:10.1016/j.ijrobp.2009.02.091
- 600 21. Serduc R, Vérant P, Vial J-C, et al. In vivo two-photon microscopy study of short-term
601 effects of microbeam irradiation on normal mouse brain microvasculature. *Int J Radiat*
602 *Oncol*. 2006;64(5):1519-1527. doi:10.1016/j.ijrobp.2005.11.047
- 603 22. Dilmanian FA, Button TM, Le Duc G, et al. Response of rat intracranial 9L gliosarcoma
604 to microbeam radiation therapy. *Neuro Oncol*. 2002;4(1):26-38.
605 doi:10.1093/neuonc/4.1.26
- 606 23. Bouchet A, Lemasson B, Le Duc G, et al. Preferential effect of synchrotron microbeam
607 radiation therapy on intracerebral 9L gliosarcoma vascular networks. *Int J Radiat*
608 *Oncol Biol Phys*. 2010;78(5):1503-1512. doi:10.1016/j.ijrobp.2010.06.021
- 609 24. Agostinelli S. Geant4—a simulation toolkit. *Nucl Instruments Methods Phys Res Sect A*
610 *Accel Spectrometers, Detect Assoc Equip*. 2003;506(3):250-303. doi:10.1016/S0168-
611 9002(03)01368-8
- 612 25. Allison J, Amako K, Apostolakis J, et al. Geant4 developments and applications. *IEEE*
613 *Trans Nucl Sci*. 2006;53(1):270-278.
614 <http://ieeexplore.ieee.org/lpdocs/epic03/wrapper.htm?arnumber=1610988>.
- 615 26. Incerti S, Baldacchino G, Bernal M, et al. The Geant4-DNA project. *Int J Model*
616 *Simulation, Sci Comput*. 2010;01(02):157-178. doi:10.1142/S1793962310000122
- 617 27. Incerti S, Ivanchenko A, Karamitros M, et al. Comparison of GEANT4 very low energy
618 cross section models with experimental data in water. *Med Phys*. 2010;37(9):4692-
619 4708. doi:10.1118/1.3476457
- 620 28. Bernal MA, Bordage MC, Brown JMC, et al. Track structure modeling in liquid water: A
621 review of the Geant4-DNA very low energy extension of the Geant4 Monte Carlo
622 simulation toolkit. *Phys Medica*. 2015;31(8):861-874. doi:10.1016/j.ejmp.2015.10.087
- 623 29. Incerti S, Kyriakou I, Bernal MA, et al. Geant4-DNA example applications for track
624 structure simulations in liquid water: A report from the Geant4-DNA Project. *Med*
625 *Phys*. 2018;45(8):e722-e739. doi:10.1002/mp.13048
- 626 30. Dingfelder M, Hantke D, Inokuti M, Paretzke HG. Electron inelastic-scattering cross
627 sections in liquid water. *Radiat Phys Chem*. 1998;53(1):1-18. doi:10.1016/S0969-

- 628 806X(97)00317-4
- 629 31. Faus-Golfe A, Mazal A, Patriarca A, et al. First Performance Calculations For Very High
630 Energy Electron Radiation Therapy Experiment At PRAE. *IPAC 2018*.:516-519.
631 doi:10.18429/JACoW-IPAC2018-MOPML051
- 632 32. Guardiola C, Peucelle C, Prezado Y. Optimization of the mechanical collimation for
633 minibeam generation in proton minibeam radiation therapy. *Med Phys*.
634 2017;44(4):1470-1478. doi:10.1002/mp.12131
- 635 33. Delorme R, Hrybok A, Faus-Golfe A, Prezado Y. EP-2198: Implementation of very high
636 energy electron grid therapy: Monte Carlo study of source definition. *Radiother Oncol*.
637 2018;127:S1214-S1215. doi:10.1016/S0167-8140(18)32507-6
- 638 34. Chetty IJ, Rosu M, Kessler ML, et al. Reporting and analyzing statistical uncertainties in
639 Monte Carlo-based treatment planning. *Int J Radiat Oncol Biol Phys*. 2006;65(4):1249-
640 1259. doi:10.1016/j.ijrobp.2006.03.039
- 641 35. Dos Santos M, Villagrasa C, Clairand I, Incerti S. Influence of the DNA density on the
642 number of clustered damages created by protons of different energies. *Nucl*
643 *Instruments Methods Phys Res Sect B Beam Interact with Mater Atoms*. 2013;298:47-
644 54. doi:10.1016/J.NIMB.2013.01.009
- 645 36. Schuemann J, McNamara AL, Warmenhoven JW, et al. A New Standard DNA Damage
646 (SDD) Data Format. *Radiat Res*. 2019;191(1):76. doi:10.1667/RR15209.1
- 647 37. Francis Z, Villagrasa C, Clairand I. Simulation of DNA damage clustering after proton
648 irradiation using an adapted DBSCAN algorithm. *Comput Methods Programs Biomed*.
649 2011;101(3):265-270. doi:10.1016/J.CMPB.2010.12.012
- 650 38. Friedland W, Schmitt E, Kundrát P, et al. Comprehensive track-structure based
651 evaluation of DNA damage by light ions from radiotherapy-relevant energies down to
652 stopping. *Sci Rep*. 2017;7(1):45161. doi:10.1038/srep45161
- 653 39. NIKJOO, P. O'NEILL, D. T. GOODHEAD H. Computational modelling of low-energy
654 electron-induced DNA damage by early physical and chemical events. *Int J Radiat Biol*.
655 1997;71(5):467-483. doi:10.1080/095530097143798
- 656 40. Bernhardt P, Friedland W, Jacob P, Paretzke H. Modeling of ultrasoft X-ray induced
657 DNA damage using structured higher order DNA targets. *Int J Mass Spectrom*.
658 2003;223-224:579-597. doi:10.1016/S1387-3806(02)00879-5
- 659 41. Chatzipapas KP, Papadimitroulas P, Obeidat M, et al. Quantification of DNA double-
660 strand breaks using Geant4- DNA. *Med Phys*. 2018;46(1):mp.13290.
661 doi:10.1002/mp.13290
- 662 42. Guardiola C, Prezado Y, Bergs JWJ. Effect of X-ray minibeam radiation therapy on
663 clonogenic survival of F98 rat glioma cells. *Clin Transl Radiat Oncol*. August 2018.
664 doi:10.1016/J.CTRO.2018.07.005
- 665 43. Frankenberg D, Frankenberg-Schwager M, Blöcher D, Harbich R. Evidence for DNA
666 double-strand breaks as the critical lesions in yeast cells irradiated with sparsely or
667 densely ionizing radiation under oxic or anoxic conditions. *Radiat Res*. 1981;88(3):524-
668 532. <http://www.ncbi.nlm.nih.gov/pubmed/7031753>. Accessed May 20, 2019.
- 669 44. Burma S, Chen BP, Murphy M, Kurimasa A, Chen DJ. ATM Phosphorylates Histone
670 H2AX in Response to DNA Double-strand Breaks. *J Biol Chem*. 2001;276(45):42462-
671 42467. doi:10.1074/jbc.C100466200
- 672 45. Friedland W, Jacob P, Bernhardt P, Paretzke HG, Dingfelder M. Simulation of DNA
673 damage after proton irradiation. *Radiat Res*. 2003;159(3):401-410.
674 <http://www.ncbi.nlm.nih.gov/pubmed/12600243>. Accessed August 6, 2019.

- 675 46. Nikjoo H, O'Neill P, Wilson WE, Goodhead DT. Computational approach for
676 determining the spectrum of DNA damage induced by ionizing radiation. *Radiat Res.*
677 2001;156(5 Pt 2):577-583. <http://www.ncbi.nlm.nih.gov/pubmed/11604075>.
678 Accessed August 6, 2019.
- 679 47. Ward JF. DNA Damage Produced by Ionizing Radiation in Mammalian Cells: Identities,
680 Mechanisms of Formation, and Reparability. *Prog Nucleic Acid Res Mol Biol.*
681 1988;35:95-125. doi:10.1016/S0079-6603(08)60611-X
- 682 48. LaVerne JA, Pimblott SM. Yields of Hydroxyl Radical and Hydrated Electron Scavenging
683 Reactions in Aqueous Solutions of Biological Interest. *Radiat Res.* 1993;135(1):16.
684 doi:10.2307/3578391
- 685 49. Tang N, Bueno M, Meylan S, et al. Influence of chromatin compaction on simulated
686 early radiation-induced DNA damage using Geant4-DNA. *Med Phys.* 2019;46(3):1501-
687 1511. doi:10.1002/mp.13405
- 688 50. Meylan S, Vimont U, Incerti S, Clairand I, Villagrasa C. Geant4-DNA simulations using
689 complex DNA geometries generated by the DnaFabric tool. *Comput Phys Commun.*
690 2016;204:159-169. doi:10.1016/J.CPC.2016.02.019
691